CrossMark

Threshold of Non-potential Magnetic Helicity Ratios at the Onset of Solar Eruptions

F. P. Zuccarello[1,2] , E. Pariat[2] , G. Valori[3] , and L. Linan[2]

[1] Centre for mathematical Plasma Astrophysics, Department of Mathematics, KU Leuven, Celestijnenlaan 200B, B-3001 Leuven, Belgium
Francesco.Zuccarello@kuleuven.be

[2] LESIA, Observatoire de Paris, Université PSL, CNRS, Sorbonne Université, Univ. Paris Diderot, Sorbonne Paris Cité, 5 place Jules Janssen, F-92195 Meudon,
France; Etienne.Pariat@obspm.fr, Luis.Linan@obspm.fr

[3] UCL-Mullard Space Science Laboratory, Holmbury St. Mary, Dorking, Surrey, RH5 6NT, UK; g.valori@ucl.ac.uk

Abstract

The relative magnetic helicity is a quantity that is often used to describe the level of entanglement of non-isolated magnetic fields, such as the magnetic field of solar active regions. The aim of this paper is to investigate how different kinds of photospheric boundary flows accumulate relative magnetic helicity in the corona and if and how well magnetic-helicity-related quantities identify the onset of an eruption. We use a series of three-dimensional, parametric magnetohydrodynamic simulations of the formation and eruption of magnetic flux ropes. All the simulations are performed on the same grid, using the same parameters, but they are characterized by different driving photospheric flows, i.e., shearing, convergence, stretching, and peripheral- and central- dispersion flows. For each of the simulations, the instant of the onset of the eruption is carefully identified by using a series of relaxation runs. We find that magnetic energy and total relative helicity are mostly injected when shearing flows are applied at the boundary, while the magnetic energy and helicity associated with the coronal electric currents increase regardless of the kind of photospheric flows. We also find that, at the onset of the eruptions, the ratio between the non-potential magnetic helicity and the total relative magnetic helicity has the same value for all the simulations, suggesting the existence of a threshold in this quantity. Such a threshold is not observed for other quantities as, for example, those related to the magnetic energy.

Key words: magnetic fields – methods: numerical – Sun: coronal mass ejections (CMEs) – Sun: flares

1. Introduction

Over the last few years, the study of magnetic helicity, a quantity estimating the level of twist and entanglement of the magnetic field lines in a magnetized plasma, has received renewed attention in solar physics. This evolution has been enabled thanks to the development of several new methods to compute and represent magnetic helicity (Rudenko & Myshyakov 2011; Thalmann et al. 2011; Valori et al. 2012; Yang et al. 2013; Yeates & Hornig 2013, 2014; Dalmasse et al. 2014; Prior & Yeates 2014). Among these new approaches, some allow us to properly compute magnetic helicity in non-magnetically isolated domains, i.e., in typical conditions for natural plasma where the magnetic field is threading the boundaries of the studied domain (see Valori et al. 2016, for a complete review and a benchmark of these methods). These new techniques now permit an exact and controlled estimation of magnetic helicity in three-dimensional (3D) data sets, and have in particular been applied to the study of the evolution of helicity in several numerical simulations of solar active events (Moraitis et al. 2014; Pariat et al. 2015, 2017; Sturrock et al. 2015; Sturrock & Hood 2016) as well as in coronal magnetic field extrapolations of observed active regions (Valori et al. 2013; Moraitis et al. 2014; Guo et al. 2017; James et al. 2018).

Magnetic helicity has recently been used as an innovative tool to study and better understand typical problems in solar physics such as the magnetic reconnection mechanism (Russell et al. 2015), the formation of filament channels (Knizhnik et al. 2015, 2017; Zhao et al. 2015) and their large-scale distribution over the solar cycle (Yeates & Hornig 2016), the solar dynamo (Miesch et al. 2016; Brandenburg et al. 2017), the formation of active regions (Liu & Schuck 2012; Liu et al. 2014a, 2014b; Moraitis et al. 2014; Pariat et al. 2017), the

rotation of sunspots (Sturrock et al. 2015; Sturrock & Hood 2016), and the generation of solar jets (Karpen et al. 2017).

A field of research in which magnetic helicity is expected to bring key results is the study of solar flares and eruptions. Even though magnetic helicity is only a strict invariant in ideal magnetohydrodynamic (MHD), Pariat et al. (2015) have confirmed Berger (1984)'s scaling argument that helicity is quasi-conserved in active events even when intense nonideal processes such as magnetic reconnection are acting to transform most of the magnetic energy. This now-demonstrated conservation of magnetic helicity is a key concept that is believed to be a ruling principle beyond the existence and the formation of coronal mass ejections (Rust & Kumar 1994; Low 1996; Green et al. 2002; Mandrini et al. 2005; Priest et al. 2016).

The study of the relationship between flare/eruptions and the magnetic evolution of active regions has been particularly prolific (e.g., Nindos & Zhang 2002; Nindos & Andrews 2004; Park et al. 2008, 2010; Zuccarello et al. 2011; Park et al. 2012; Tziotziou et al. 2012, 2013, 2014; Zuccarello et al. 2014, 2017). So far, most of the work has relied on computing magnetic helicity from observed series of magnetograms and estimating the helicity flux following the ground breaking method of Chae (2001), which has, however, some inherent limitations (Démoulin & Pariat 2009). It is nonetheless worth mentioning that several such observational studies have concluded on a close relation between high helicity content and enhanced eruptivity (e.g., Nindos & Andrews 2004; LaBonte et al. 2007; Smyrli et al. 2010; Tziotziou et al. 2012).

The new and exact methods to compute helicity in a 3D domain are however now enabling the comprehensive study of magnetic helicity in numerical data sets. Pariat et al. (2017)

have recently studied parametric simulations of the formation of solar active regions leading either to stable configurations or to eruptions (presented in Leake et al. 2013, 2014). They found that magnetic helicity was strongly discriminating between the different simulations. Furthermore, they showed that by using the helicity decomposition introduced by Berger (2003), the ratio of the magnetic helicity of the current-carrying part of the field to the total helicity could be used as a clear predictor of the eruptivity in the simulations. This quantity indeed presented high values only for the eruptive simulations and only before the eruption. Additionally, this helicity ratio was no longer differentiating the eruptive simulation from the non-eruptive one after the eruption, when the system was stable in all of the different runs.

The experimental set-up of Leake et al. (2013, 2014) does not permit one to determine the existence of an eruptivity threshold related to the helicity ratio. The stability of the magnetic system was indeed likely deterministically given by the initial condition, i.e., for the eruptive simulations, the system was not brought from an equilibrium stage toward instability by controlled imposed quasi-steady forcing. Therefore, while remarkable, the results of Pariat et al. (2017) were not conclusive on the reason why the helicity of the current-carrying part of the field could be related to an enhanced eruptivity. In order to determine whether their results were due to pure hazard or were symptomatic of a deeper physical meaning, the present study investigates the energy and helicity content of a radically different set of parametric simulations of eruptive events. This manuscript focuses on the analysis of the line-tied 3D MHD simulations of Zuccarello et al. (2015). In these simulations, eruptions are triggered by boundary-driven motions that mimic the long-term evolution of solar active regions, with the presence of shearing motions and large-scale diffusion of the magnetic polarities. Unlike with the flux-emergence simulations of Leake et al. (2013, 2014), the trigger time and mechanism have been carefully determined by performing numerous relaxation runs. Zuccarello et al. (2015) have shown that the eruptions were tightly related with the torus instability mechanism (Kliem & Török 2006; Török & Kliem 2007; Aulanier et al. 2010; Démoulin & Aulanier 2010; Olmedo & Zhang 2010; Kliem et al. 2014). A goal of the present study is to determine whether a helicity-based eruptivity predictor is also able to describe the eruptivity stage of the simulations of Zuccarello et al. (2015) and how it relates with the torus instability.

Additionally, the parametric simulations of Zuccarello et al. (2015) present different types of boundary-driving motions. Thanks to the comparison of these different simulations, it is possible to compare and determine which boundary motions are the most efficient at injecting total helicity in the coronal domain, as well as in the different terms of the helicity decomposition. Helicity accumulation is indeed a fundamental process of the formation and evolution of active regions (Green et al. 2002, 2003; Mandrini et al. 2005; Liu & Schuck 2012; Liu et al. 2014a, 2014b; Romano et al. 2014; Sturrock et al. 2015; van Driel-Gesztelyi & Green 2015; Sturrock & Hood 2016). Studying the most efficient way by which helicity is injected in active regions can reveal information that is particularly important for determining their eruptivity potential.

The manuscript is organized as follows. The simulation setups and evolution of the system are discussed in Section 2.

The different magnetic energy and helicity decompositions are presented in Section 3. Section 4 describes the evolution of the magnetic flux as a result of the applied boundary motions. Sections 5 and 6 present the results of our analysis, i.e., the time evolution of the different magnetic energy and helicity decompositions and their values at the onset of the eruptions. Finally, in Section 7, we discuss our results and conclude.

2. The MHD Simulations

To study the evolution of magnetic energy and helicity during the formation and eruption of magnetic flux ropes, we solve the full three-dimensional MHD equations using the OHM-MPI code (Aulanier et al. 2005; Zuccarello et al. 2015). In this paper, we analyze the same runs presented in Zuccarello et al. (2015) where the MHD equations are solved in a nonuniform Cartesian grid that expands from the location $x = y = z = 0$ and covers the domain $x \in [-10, 10]$, $y \in [-10, 10]$, $z \in [0, 30]$ where x and y are the horizontal directions and z is the vertical one. The goal of that study was to carefully determine and investigate the onset of the eruptions in the framework of the torus instability. To achieve this goal, a parametric study consisting of four different simulations was performed. For each of the four different simulations, the time of the onset of the eruption was carefully determined using a series of relaxation runs.

The four simulations share the same initial phase where the magnetic field is modified from an initial, potential configuration into a sheared one (Sections 2.1 and 2.2). From this point onward, four different boundary motions that result in four different ways to build a flux rope and bring it to the eruption point are applied (Section 2.4). Finally, a proper eruption phase follows in each of the four runs (Section 2.5). The first two phases, shearing and flux rope formation, are the most relevant ones for the study of helicity evolution discussed in this article.

2.1. Initial Condition

The initial condition for the magnetic field, common to all simulations, consists of an asymmetric and bipolar active region generated by two unbalanced sub-photospheric monopoles (see Figure 1, left panel). In the non-dimensional units of the simulation (cf. Section 2.4 of Aulanier et al. 2010, for a possible choice of dimensional units), the initial density in the volume is $\rho(t = 0) = B^2(t = 0)$, such that the initial Alfvén speed is $c_A(t = 0) = 1$, while the initial velocity field is $\boldsymbol{u}(t = 0) = 0$.

We impose "open" boundary conditions for all of the boundaries apart from the boundary at $z = 0$, i.e., the photospheric boundary, where line-tied boundary conditions are applied instead (Aulanier et al. 2005). We notice that, as a result of the applied boundary motions and field dynamics, the configuration of the field is naturally expanding and flux is free to leave the simulation box trough lateral and top boundaries throughout the simulations.

2.2. The Common Shearing Phase

For all of the simulations, the initial potential magnetic field is evolved into a current-carrying magnetic field by imposing asymmetric vortices centered around the local maxima of $|B_z(z = 0)|$.
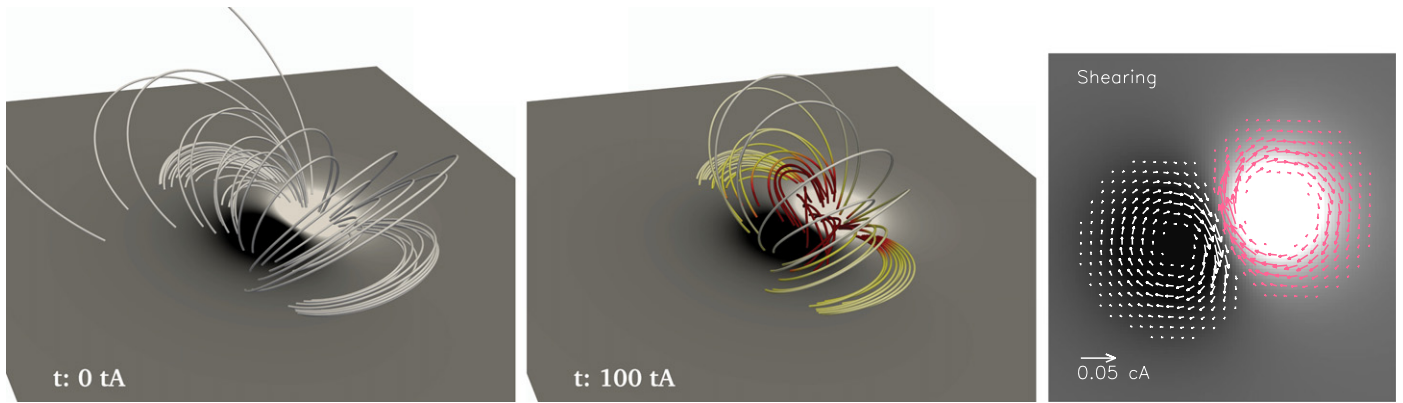
Figure 1. Evolution of the magnetic field for the shearing phase common to all the simulations (left and middle panels) and the applied boundary motions (right panel). The magnetic field lines are color coded with the current density, where yellow/red means higher current density. White/black indicate positive/negative $B_z(z = 0)$, respectively. White/magenta arrows indicate flows applied to the negative/positive polarity.

Figure 1 (right panel) shows the applied flow field. By design, these boundary flows induce shear close to the polarity inversion line (PIL) of the active region and affect the periphery of the active region only mildly. Moreover, the flows are tangent to the iso-contours of $B_z(z = 0)$; therefore, during this phase, the distribution of B_z at the photospheric boundary $z = 0$ remains unchanged. Because the major component of the flow field during this phase consists of shearing motions close to the PIL, we refer to this phase as the shearing phase and to these motions as shearing motions.

The shearing flows are applied from $t \simeq 10t_A$ until $t \simeq 100t_A$. At the end of this phase, the magnetic field configuration is characterized by a highly sheared, current-carrying magnetic arcade surrounded by a quasi-potential background field anchored around the center of the magnetic polarities (see Figure 1, middle panel).

To ensure that the normal component of the magnetic field at the boundary remains unchanged, during this phase the photospheric diffusion is set to $\eta_{\mathrm{phot}} = 0$. The coronal diffusion and pseudo-viscosity are set to $\eta_{\mathrm{corona}} = 4.8 \times 10^{-4}$ and $\nu' = 25$, respectively (see Section 2.3 of Zuccarello et al. 2015).

2.3. Control Case: The Non-eruptive Run

As a term of comparison throughout this paper, we also include a non-eruptive control run obtained by avoiding the photospheric driving phase of Section 2.4. For this run, at the photospheric boundary we impose $\boldsymbol{u}(t \gtrsim 100t_A) = 0$ and $\eta_{\mathrm{phot}} = 4.8 \times 10^{-4}$ for $100t_A \lesssim t \lesssim 164t_A$ and $\eta_{\mathrm{phot}} = 0$ for $t \gtrsim 164t_A$. The coronal diffusion and pseudo-viscosity are the same as those for the shearing phase for $100t_A \lesssim t \lesssim 164t_A$ and they are increased by a factor 4.37 and 1.67, respectively for $t \gtrsim 164t_A$.

The diffusion and pseudo-viscosity parameters have the same time dependence as the other four simulations runs. This allows us to distinguish the effects of direct diffusion, which we expect to be similar for identical parameters, from the run-specific dynamic due to different evolution of energy and helicity.

2.4. The Flux-rope Formation Phases

From $t \simeq 105t_A$, the flux rope formation phase starts. During this phase, at the line-tied boundary we apply four different types of photospheric motions.

Figure 2 (bottom panels) shows the applied boundary motions. The four different velocity fields aim to mimic flow patters typically observed on the Sun. The four different velocity fields result in four different simulations runs labeled as "Convergence", "Stretching", "Dispersion Peripheral" (Disp. Periph.), and "Dispersion Central" (Disp. Cent.).

The run labeled "Convergence" is characterized by flows that only have a horizontal component and are applied only in the proximity of the PIL. These flows result in the advection of photospheric magnetic field toward the PIL, but do not affect the central and peripheral parts of the active region.

In the run labeled "Stretching", the flows are now applied not only in the proximity of the PIL but also in the periphery of the active region. The effect of these flows is to induce an asymmetric stretching of $B_z(z = 0)$.

Finally, the runs labeled as "Disp. Periph." and "Disp. Cent." are characterized by flows that spreads radially from the center of the magnetic polarities. The difference between the two flow patterns is the size of the portion of the magnetic polarities that is affected by the flow. In "Disp. Periph.", only the periphery of the magnetic polarities is subjected to the flows, resulting in a peripheral dispersion of the magnetic field, while in "Disp. Cent.", a larger region of the polarity is subjected to these flows, resulting in a more significant diffusion of the magnetic polarities.

Figure 2 (bottom panels) shows that all of the flows have a component that advects oppositely directed vertical magnetic field toward the PIL. To allow the cancellation of this oppositely directed magnetic flux, during this phase the photospheric diffusion is set to $\eta_{\mathrm{phot}} = 4.8 \times 10^{-4}$. The coronal diffusion and pseudo-viscosity are kept the same as in the shearing phase.

The response of the solar corona to the applied boundary flows for the "Disp. Periph." run is shown in Figure 2 (top panels). As a consequence of the cancellation of magnetic flux around the PIL, a magnetic flux rope is formed through magnetic reconnection at a bald-patch separatrix (Démoulin et al. 1996). This reconnection process transfers sheared, arcade-like magnetic flux into the flux rope, eventually increasing the total current within it, and driving its slow rise up to a point when the torus instability sets in and the flux rope undergoes a full eruption. A similar mechanism yields the formation of a flux rope in the other runs as well (see Zuccarello et al. 2015, for additional details). The flux rope
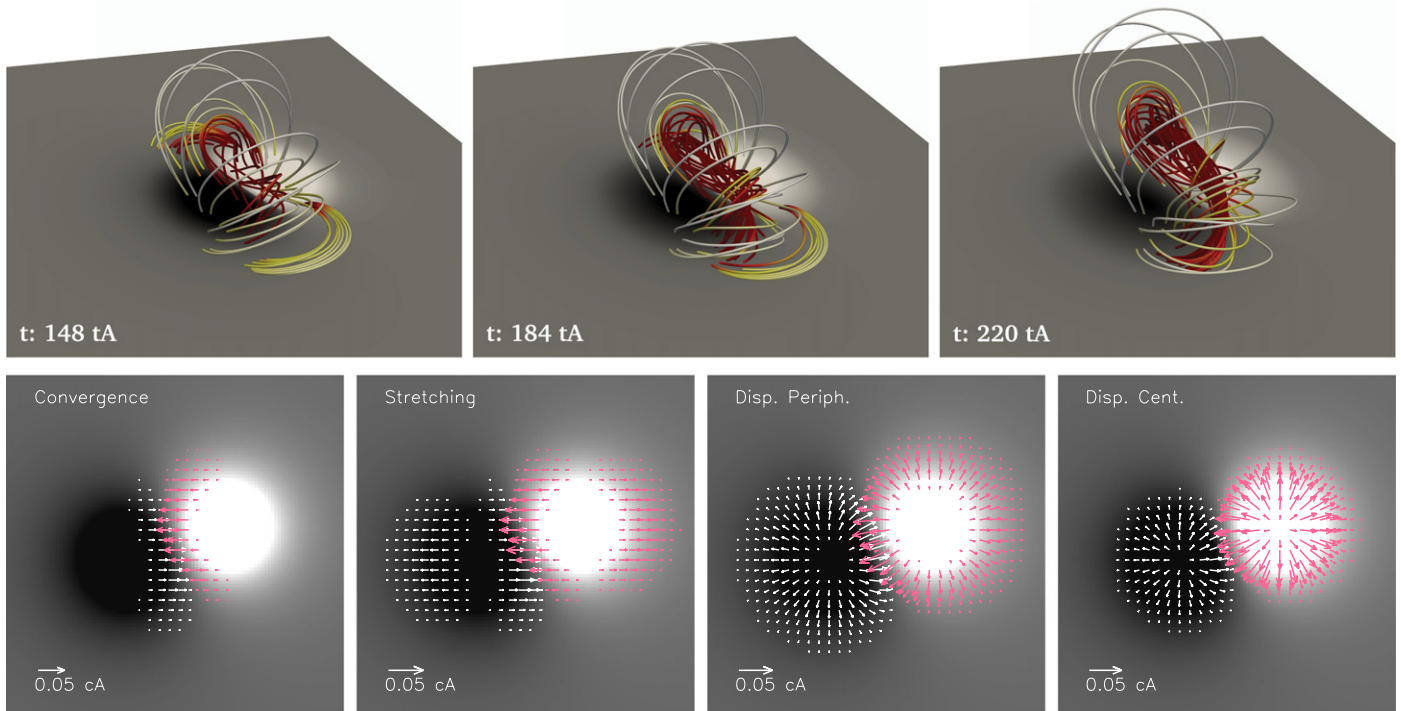
Figure 2. Evolution of the magnetic field for the Dispersion Peripheral run during the flux rope formation phase (top panels) and the applied boundary motions (bottom panels) for the four different simulations runs. The color scheme is the same as in Figure 1.

formation phase ends at the time of the eruption, which happens at a different time in the four simulations.

2.5. The Eruption Phase

The onset of the torus instability is determined through a series of relaxation runs in which the photospheric boundary flows are gradually re-set to zero using a ramp-down time profile of total time width $\Delta t = 6t_A$.

In other words, for each of the four experimental set-up, dozens of simulations have been performed in which the applied flows were imposed for different durations before being smoothly stopped. Only when the boundary flow was imposed long enough, a marked eruption was observed. If the boundary flows are stopped before the instant t_I, the system either relaxes to a new equilibrium or the flux rope undergoes an extremely deflected eruption (see Zuccarello et al. 2015, for additional details). However, if the boundary flows are stopped at (or after) t_I, the flux rope undergoes a full eruption and expands in the numerical domain. As the four simulations have different photospheric flow evolutions, the exact time at which the instability sets in is different for the four cases. By stopping the photospheric driver at different instants in time and letting the system evolve under the effect of the residual Lorentz force, Zuccarello et al. (2015) have shown that the onset of the instability leading to full eruptions occurs at $t_I = 196, 214, 220$ and $164t_A$ for the "Convergence", "Stretching", "Disp. Periph.", and "Disp. Cent." runs, respectively. It should be noted that the time t_I corresponds to the middle of the ramp-down time profile; therefore, the boundary flows are zero only for $\bar{t}_I \gtrsim t_I + 3t_A$. The vertical lines in all the Figures of the present paper indicate the time $\bar{t}_I$.

By using the same ramp-down time profile, at time t_I we also re-set the photospheric diffusion to zero. For numerical stability reasons, at the same time t_I and by using a similar ramp-up time

profile, we increase the coronal diffusion by a factor 4.37 and the pseudo-viscosity by a factor 1.67. Because we focus on the triggering of the instability, in the following, only the evolution until $10t_A$ after the time $\bar{t}_I$ of each simulation is shown. However, all simulations were continued for long after that time (see Zuccarello et al. 2015).

3. Magnetic Helicity and Energy Decompositions

The magnetic helicity H of a magnetic field $\boldsymbol{B}$ in a volume $\mathcal{V}$ is defined as:

$$H = \int_{\mathcal{V}} \boldsymbol{A} \cdot \boldsymbol{B} \, d\mathcal{V}, \tag{1}$$

where $\boldsymbol{A} = \nabla \times \boldsymbol{B}$ is the vector potential. This quantity is gauge invariant only when the magnetic field $\boldsymbol{B}$ is fully contained inside the volume $\mathcal{V}$, e.g., when the magnetic field is tangential to the surface $\partial\mathcal{V}$ that bounds $\mathcal{V}$. This condition is rarely satisfied in the magnetic field systems that are of interest in solar physics, i.e., open coronal volumes.

Following the work of Berger & Field (1984), Finn & Antonsen (1985) showed that in the case where $\boldsymbol{B}$ is not fully contained in $\mathcal{V}$, a quantity that is gauge invariant by definition and it is better suited to characterize the system, is the relative magnetic helicity:

$$H_V = \int_{\mathcal{V}} (\boldsymbol{A} + \boldsymbol{A}_p) \cdot (\boldsymbol{B} - \boldsymbol{B}_p) \, d\mathcal{V}, \tag{2}$$

with $\boldsymbol{A}_p$ the vector potential of the potential field $\boldsymbol{B}_p = \nabla \times \boldsymbol{A}_p$ that has the same distribution of the normal component of $\boldsymbol{B}$ on the bounding surface.

A possible decomposition of Equation (2) is (Berger 2003):

$$H_V = H_j + H_{pj}, \quad \text{with} \tag{3}$$

$$H_j = \int_{\mathcal{V}} (\boldsymbol{A} - \boldsymbol{A}_p) \cdot (\boldsymbol{B} - \boldsymbol{B}_p)\, d\mathcal{V}, \tag{4}$$

$$H_{pj} = 2 \int_{\mathcal{V}} \boldsymbol{A}_p \cdot (\boldsymbol{B} - \boldsymbol{B}_p)\, d\mathcal{V}, \tag{5}$$

where H_j is the magnetic helicity of the non-potential, or current-carrying, component of the magnetic field, $\boldsymbol{B}_j = \boldsymbol{B} - \boldsymbol{B}_p$, and H_{pj} is a volume-threading term involving both $\boldsymbol{B}_p$ and $\boldsymbol{B}_j$. Because $\boldsymbol{B}$ and $\boldsymbol{B}_p$ have the same normal distribution on $\partial\mathcal{V}$, both H_V, H_j and H_{pj} are separately gauge invariant. Similarly to (Pariat et al. 2017, cf. Section 4.1), in the present paper, the quantities $\boldsymbol{B}_p$, $\boldsymbol{A}_p$, and $\boldsymbol{A}$ are computed using the method of Valori et al. (2012).

The different flux rope formation phases are associated with different photospheric boundary motions that result in different evolutions of $B_z(z = 0)$. As a result, the magnetic flux is different for the different simulations. In order to account for these differences when comparing the various helicity decompositions at the moment of the eruption we consider their normalized value, i.e., $H_V(t)/\Phi^2(t)$, $H_j(t)/\Phi^2(t)$ and $H_{pj}(t)/\Phi^2(t)$, where $\Phi(t) = \frac{1}{2} \int_{z=0} |B_z(z = 0, t)|\, dxdy$.

In the present paper, the different decompositions of the magnetic energy are computed following the approach discussed in Valori et al. (2013), where the magnetic energy of a magnetic field with finite non-solenoidality ($\nabla \cdot \boldsymbol{B} \neq 0$), can be decomposed as:

$$E_V = E_p + E_j + E_{ns}, \tag{6}$$

where E_p and E_j are the energies associated with the potential and current-carrying solenoidal contributions, and E_{ns}, is the sum of the artifact non-solenoidal contributions (see Equations (7), (8) in Valori et al. 2013, for the corresponding expressions). For purely solenoidal fields E_{ns} is zero, however, finite non-solenoidality is generally present when discrete numerical meshes are considered. As discussed in Valori et al. (2016), the non-solenoidality of the field actually affects the precision of the helicity computations. For the simulations presented here, the average non-solenoidality is $E_{ns}/E_V \simeq 0.02$. We note that in order to apply the method of Valori et al. (2012), the nonuniform grid used to perform the simulations has been interpolated into a uniform grid, and the divergence values are increased by the interpolation. While these values are not representative of the quality of the simulations themselves, they nevertheless allow us to estimate the precision of the magnetic helicity computations discussed here. According to the results of Valori et al. (2016), the precision of our helicity computations is $\lesssim 2\%$.

4. Evolution of the Magnetic Flux

The evolution of the photospheric magnetic flux as a function of time and, for all the simulation runs, is presented in Figure 3. The magnetic flux is constant during the common shearing phase. This is a consequence of the design of the boundary motions, which do not change the phostospheric
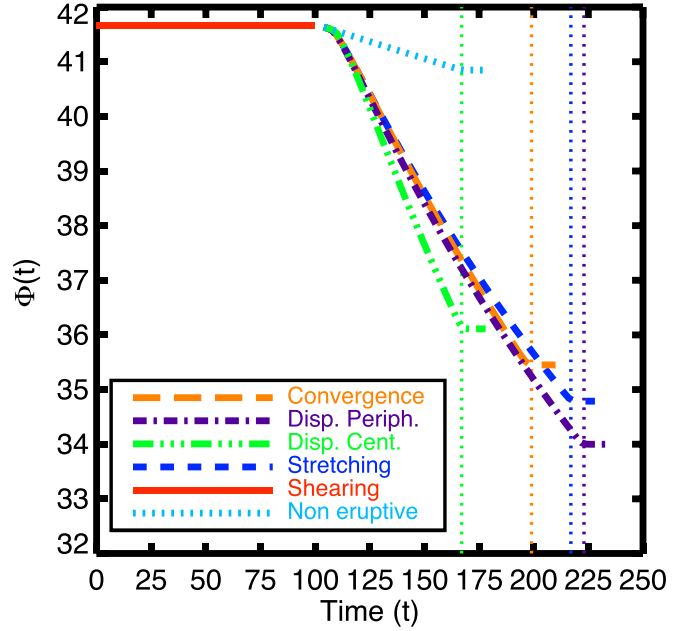

Figure 3. Time evolution of the photospheric magnetic flux for the common shearing phase (red), for the non-eruptive run (cyan), and for the four eruptive runs.

distribution of B_z, and of the fact that the photospheric diffusion is $\eta_{phot} = 0$ during this phase.

In the control non-eruptive run, where the flows are set to zero and only a finite photospheric diffusion is imposed at the boundary, only $\lesssim 2\%$ of the initial photospheric flux is diffused within $\sim 60\, t_A$.

During the flux rope formation phase, opposite magnetic flux is advected toward the PIL in all four simulations. Combined with a finite photospheric diffusion, this results in the cancellation of about 13%–18% of the initial photospheric flux at the moment of the onset of the eruption.

From $\bar{t}_I$, both photospheric flows and diffusion are re-set to zero, and the photospheric flux remains constant until the end of the simulation.

The change in the slope of the photospheric flux that we observe toward the end of the flux rope formation phases in Figure 3 is essentially due to the change in the forcing of the bottom boundary of the simulation, as is expected considering that this quantity is only measured at this boundary, and does not allow one to discern the moment of the onset of the instability.

Finally, we note that at the moment of the eruption, the different runs have reached different values of the magnetic flux.

5. Trends in Magnetic Energy and Helicity

In this Section, we discuss the trends in the time evolution of the magnetic energy and of the magnetic helicity for the different runs.

5.1. Comparison between the Shearing and Flux-rope Formation Phases

Figure 4 (top panels) shows the evolution of the different energy decompositions. During the common shearing phase, i.e., from $t \simeq 10 t_A$ to $t \simeq 100 t_A$, E_V shows a linear increase up to about 37% of its initial value. A comparison between E_j and
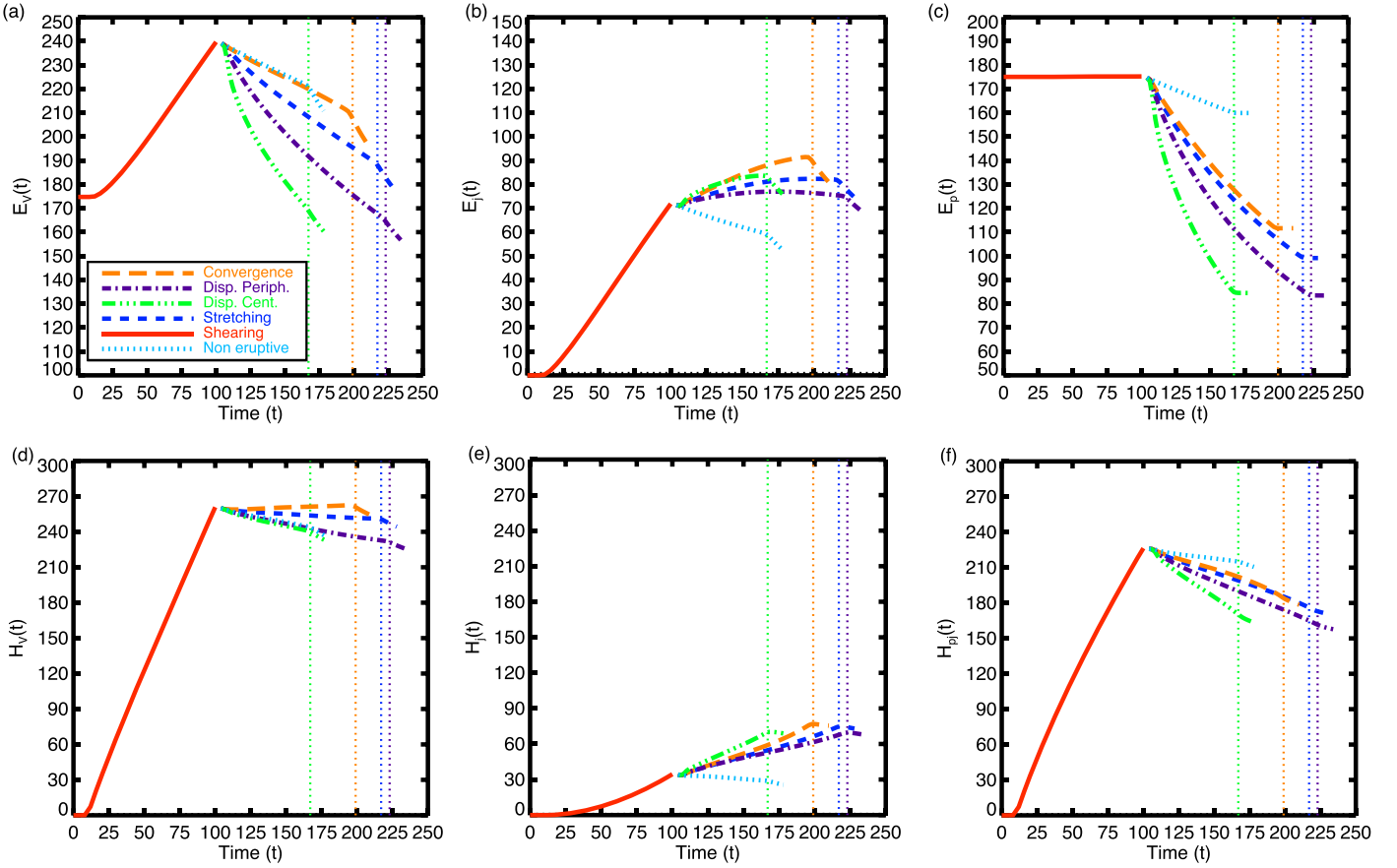
Figure 4. Time evolution of the different energy (top) and helicity (bottom) terms for the shearing and flux rope formation phases.

E_p (Figures 4(b) and (c)) shows that the increase in E_V is due to the increase of E_j. This is expected, as the shearing flows are designed in such a way to not change the boundary distribution of B_z, and, hence, of E_p.

In the control non-eruptive run, from $t \simeq 105t_A$ onward, all of the different energy decompositions display a decrease due to the finite photospheric and coronal diffusion. After $t \simeq 164t_A$, E_V and E_j continue to decrease even faster (the coronal diffusion is further increased during this phase, see Section 2.3), while E_p is now constant, as η_{phot} is re-set to zero during this phase.

During the different flux rope formation phases, i.e., from $t \simeq 105t_A$ to $t \simeq t_I$, E_V decreases, and this is the case up to the end of the simulations (not shown in the Figure). Despite the total magnetic energy decreases, Figure 4(b) shows that, apart from the control case, E_j actually increases during the flux rope formation phase, up to the time $t \simeq t_I$, where it reaches a maximum and starts to decrease. Figure 4(c) shows that E_p decreases during the flux rope formation phase, suggesting that the major reason of the energy decrease during the flux rope formation phase is due to a decrease of E_p.

A comparison between the shearing and the flux rope formation phases shows that the major injection of E_j occurs during the shearing phase; the rate of increase of E_j during the shearing phase is between ~ 4.5 and ~ 54 times higher than its rate of increase during the flux rope formation phase.

The time evolution of H_V is shown in Figure 4(d). During the common shearing phase, H_V steadily and linearly increases with time. This trend changes during the flux rope formation phase, when the total helicity is either roughly constant or

slightly decreases. This is true until the end of simulations (not shown in the Figure). The situation is different when only the current-carrying component of the helicity, i.e., H_j, is considered (Figure 4(e)). Similarly to H_V, H_j also increases during the shearing phase but with a profile that is somehow different. The linear increasing phase starts with a delay of about 10–$15 \, t_A$ with respect to H_V.

Figure 4(e) shows that from $t \simeq 105t_A$ onward, for the control run, H_j is either constant or decreases. The situation is different for the other runs, where during the flux rope formation phase H_j continues to increase up to $\bar{t}_I$. Figure 4(e) also shows that H_j increases at a comparable rate both during the shearing and the flux rope formation phases.

The evolution of H_{pj} is shown in Figure 4(f). Similarly to H_V, during the shearing phase, H_{pj} steadily increases in time, accounting for the major part of the helicity injection during this phase. From $t \simeq 105t_A$ onward, H_{pj} for the control run is either constant or decreases. While the other runs also show the same trend, their respective decrease of H_{pj} is more significant than the one observed for the control run. Therefore, the decrease of H_{pj} during the flux rope formation phase is not only due to the finite diffusion, but likely to a re-distribution of the relative helicity between its different component H_j and H_{pj} (cf. L. Linan et al. 2018, in preparation).

To summarize, the analysis shows that: (1) the largest injection of total magnetic energy and relative magnetic helicity occurs during the shearing phase; (2) during the shearing phase, E_j increases as it is the case for H_{pj}, i.e., magnetic energy and helicity behave differently during this phase; (3) at the end of shearing phase, E_V is dominated by E_p, and H_V is dominated by
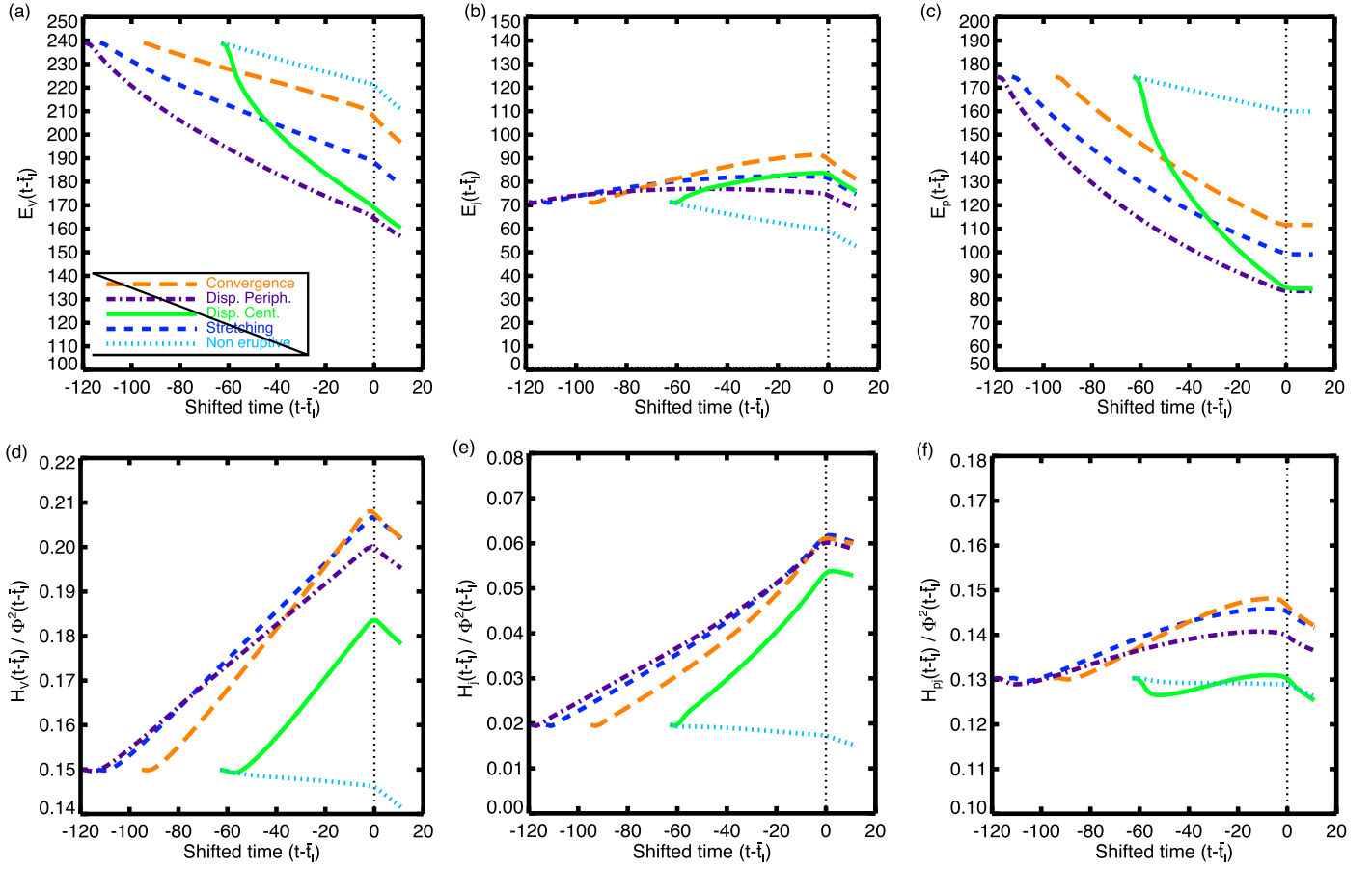
Figure 5. Time evolution of the different energy (top) and normalized-helicity (bottom) terms during the flux rope formation phase. The timescale is shifted so that the time are given with respect to $\bar{t}_I$.

H_{pj}, i.e., magnetic energy and helicity are similar in this aspect; (4) in the flux rope formation phase, both E_V and H_V decrease, both E_p and H_{pj} decrease, and both E_j and H_j increase, i.e., they behave similarly, unlike during the shearing phase; (5) H_j is injected with roughly the same rate during the shearing and flux rope formation phases, while this is not the case for E_j where the most of the injection occurs during the shearing phase; (6) overall, the flux rope formation phase has helped to strengthen the non-potentiality of the field and its relative portion in both E_V and H_V budgets; at the end of the flux rope formation phase, both E_j/E_V and H_j/H_V have increased compared to their values at the start of this phase (see Section 6).

5.2. Role of the Different Boundary Flows during the Flux-rope Formation Phase

In this Section, we compare the evolution during the different flux rope formation phases, focusing on the similarities and differences between them.

Figure 5 (top panels) shows the evolution of the different energy decompositions during the flux rope formation phases. In order to facilitate the comparison, the curves in Figures 5 and 6 are shifted such as to align the eruption times. The total magnetic energy, E_V, decreases for all the runs including the non-eruptive one (see Figure 5(a)). However, the "Disp. Cent." run, which is the run where the major part of the active region is subjected to the convergence flows, displays the fastest decrease of E_V, while the "Convergence" run, where only the portion of the

active region closets to PIL is subjected to the convergence motions, shows the slowest decrease of E_V. The latter is actually comparable to the decrease of E_V for the control run, where no flows are applied and the energy dissipation is only due to the coronal and photospheric diffusion.

The time evolution of E_j is shown in Figure 5(b). A clearer distinction in the trends is visible between the eruptive runs and the non-eruptive one. For the eruptive simulations, E_j increases up to the moment of the eruption, while it is always decreasing for the non-eruptive run. Differently from E_V, E_j for the "Convergence" and "Disp. Cent." runs follows a very similar trend, despite the fact that these two runs are the ones with the most different flows. Figure 5(b) shows that E_j starts to decrease after the onset of the eruption when driving flow is terminated and coronal dissipation is increased four-fold. A similar initial decrease is also observed for the control run as soon as the system is allowed to relax under the effect of the increased coronal diffusion.

Figure 5(c) shows that, during the flux rope formation phase, E_p decreases. Furthermore, the different curves are ordered in the same way as the ones of E_V, confirming that the major decrease of magnetic energy during the flux rope formation phase is due to the decrease of the energy associated with the potential magnetic field.

The time evolution of the different normalized-helicity decompositions is presented in Figure 5 (bottom panels). Globally, H_V/Φ^2 and H_j/Φ^2 show similar trends and clearly allow one to distinguish between the eruptive and non-eruptive runs; the two quantities increase for the eruptive runs, while
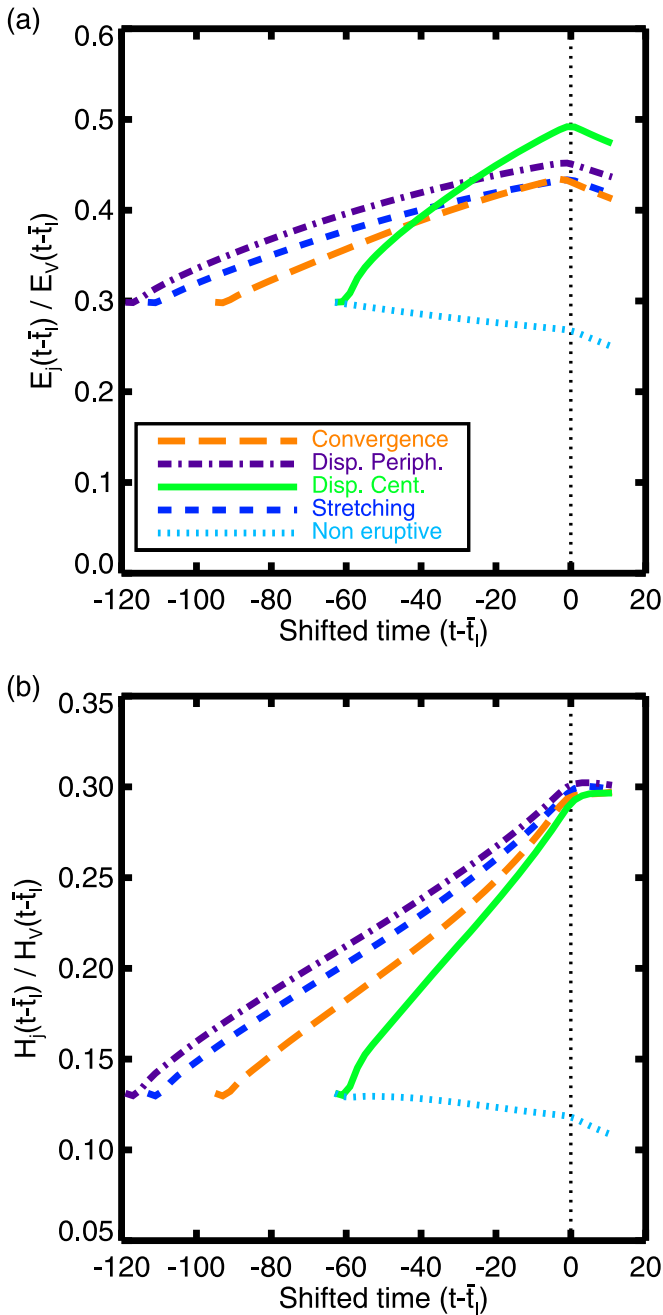
(a)

(b)

Figure 6. Time evolution of the E_j/E and H_j/H_V ratios around the onset of the eruptions.

difference is at the periphery of the active region where part of the overlying magnetic flux is anchored. This seems to suggest that even the evolution of H_j, which is in principle only related to the current-carrying part of the magnetic field, seems to be affected by the evolution of the background field. This is an example of the nonlocal character of the magnetic helicity. This result is also consistent with the analysis of the time evolution of H_j and H_{pj} of L. Linan et al. (2018, in preparation), which indicates that H_j is usually not evolving because of boundary flux but is rather transformed from H_{pj}.

Finally, Figure 5(f) shows that H_{pj}/Φ^2 initially decreases during the first stages of the convergence phase and then steadily increases up to a few Alfvén times before the onset of the instability. This behavior is observed for all of the eruptive runs, even if the "Disp. Cent." run shows a proportionally larger (smaller) decrease (increase) during the early (main) stage of the convergence phase.

To summarize, the analysis shows that (1) apart from a single case (H_{pj}/Φ^2 for the "Disp. Cent." run), the time evolution of all the different helicity terms shows a difference between the eruptive and non-eruptive runs, (2) this is not the case for the different magnetic energy terms, where only E_j shows a different trend. (3) At the time of the onset of the eruption, a change in the trend is observed for all of the simulation runs (apart from E_V for the "Disp. Cent." run). The fact that this change in trend is also observed for the control, non-eruptive run suggests that the change in the coronal diffusion and in the boundary motions at the time of the eruption (see Section 2) may play an important role.

6. Thresholds in Magnetic Energy and Helicity

In the previous Section, we investigated the evolution of different magnetic-energy and helicity-related quantities around the moment of the onset of the torus instability, and we have discussed how a change in the trend of the different curves that occurs at $t \simeq t_I$, may be somehow related to these imposed boundary conditions. This is the reason why, for any given quantity, the existence of a threshold at the moment of the onset of the instability may be more important than a change in its trend.

Zuccarello et al. (2015) analyzed these simulations in the framework of the torus instability. In this framework, the instability occurs when the flux rope axis reaches a height where the decay index of the magnetic field has a critical value that depends on the particular magnetic field configuration. For these parametric simulations, Zuccarello et al. (2015) have shown that when an eruption occurs, all of the flux ropes have reached heights where the decay index n has a critical threshold value of $n \simeq 1.45 \pm 0.05$.

The aim of this Section is to investigate if a critical threshold value in any of the different energy and helicity decompositions exists. Said differently, we investigate whether or not any of the different energy and helicity decompositions have the same value (for all the simulations) when the instability sets in and the eruptions occur. The values of the different quantities around the time of the onset of the eruption are reported in Table 1.

6.1. Magnetic Energy and Helicity Terms

Figure 5(a) shows that no threshold in the total magnetic energy exists at the moment of the eruption. More

they are roughly constant (although decreasing, largely because of the finite coronal diffusion) for the non-eruptive run. This is true until $t \simeq t_I$ when H_V/Φ^2 and H_j/Φ^2 start to decrease for all the runs (including the control run) as a consequence of the increased coronal diffusion.

A closer look at Figure 5(e) shows that, while the different curves follow a very similar trend, some differences exist. An interesting result can be found by comparing the "Stretching" and "Convergence" runs. For these two runs, the same photospheric motions profile is applied close to the PIL, and the difference only involves the periphery of the active region (see Figure 2, bottom panels). As a result, sheared arcade flux is advected toward the PIL and eventually converted into flux rope's flux, in a similar fashion for the two runs. The only

Table 1
Values of the Different Energy and Helicity Terms at the Moment of the Onset of the Instability

Run	t_I (t_A)	Φ	E_V	E_p	E_j	E_j/E_V	H_V	H_j	H_{pj}	H_j/H_V
Convergence	196	35	206.5	114.7 $\pm$ 3.1	91.8 $\pm$ 3.1	0.444 $\pm$ 0.015	260 $\pm$ 5	77 $\pm$ 5	183 $\pm$ 5	0.296 $\pm$ 0.012
Stretching	214	35	187.4	102.8 $\pm$ 3.6	84.6 $\pm$ 3.6	0.451 $\pm$ 0.019	250 $\pm$ 5	75 $\pm$ 5	175 $\pm$ 5	0.300 $\pm$ 0.012
Dispersion Peripheral	220	34	163.7	86.8 $\pm$ 3.3	76.9 $\pm$ 3.3	0.470 $\pm$ 0.020	231 $\pm$ 5	70 $\pm$ 5	161 $\pm$ 5	0.303 $\pm$ 0.012
Dispersion Central	164	36	168.1	85.1 $\pm$ 0.4	83.1 $\pm$ 0.4	0.494 $\pm$ 0.002	239 $\pm$ 5	70 $\pm$ 5	169 $\pm$ 5	0.292 $\pm$ 0.012

Note. The value of the different quantities are given at $\bar{t}_I \gtrsim t_I + 3t_A$, i.e., after the boundary motions are re-set to zero.

specifically, Table 1 shows that E_V varies from about 163.7 for the "Disp. Periph." run to about 206.5 for the "Convergence" run. The dispersion of the values, evaluated as $(\max[E_V(\bar{t}_I)] - \min[E_V(\bar{t}_I)])/\max[E_V(\bar{t}_I)]$, is too large to correspond to an instability threshold solely based on that quantity. Indeed, if such a threshold existed and corresponded to $\max[E_V(\bar{t}_I)] = 206.5$, then no eruption should have been observed for all the simulations but the "Convergence" run, as their E_V did not reach that threshold value. If the instability threshold was equal to $\min[E_V(\bar{t}_I)] = 163.7$, then the eruption time, $t \simeq t_I$ should have been different, as all simulations but the "Disp. Cent." run would have reached that value of E_V earlier than their corresponding t_I.

For the type of numerical experiment presented here, in which the system is dynamically evolved from a stable to a unstable stage, the existence of an instability threshold uniquely based on a given quantity, Q, necessarily implies that the value of $Q(\bar{t}_I)$ should be the same for all the eruptive simulations. The measurement of the dispersion of $Q(\bar{t}_I)$ between the eruptive runs (as done above), is thus a way to state the existence of a threshold for that quantity. The dispersion of about 20% obtained for E_V disqualifies the existence of a threshold based on that quantity.

A similar conclusion can be drawn also for E_j (Figure 5(b)). At the moment of the onset of the eruption, E_j has different values for the different runs with a range of dispersion of about 17% of E_j of the Convergence run. Therefore, E_j also does not allow one to determine the onset of the instability. The discrepancies are even larger when the potential magnetic energy, E_p, is considered (Figure 5(c)).

Figure 5 (bottom panels) shows that no threshold exists also for the different decompositions of the normalized magnetic helicity. However, a closer inspection of the Figure and of Table 1 show that the dispersion of the different helicity and normalized-helicity terms is within 13% (9% for H_j), i.e., the dispersion between the different helicity curves is about half the dispersion of the total energy curves.

6.2. Current-carrying to Total Magnetic Energy and Helicity Ratios

Pariat et al. (2017) have shown that the ratio E_j/E_V is a possible good eruption proxy, in the sense that it could discern between erupting and non-erupting runs. The same authors have shown that a significantly better proxy is the ratio of the helicity of the current-carrying part of the magnetic field to the total magnetic helicity, H_j/H_V, in the sense that this proxy has consistently larger values before the eruption for eruptive runs

than for non-eruptive and, after the eruption, the proxies of eruptive and non-eruptive are indistinguishable.

The time evolution of the E_j/E_V and H_j/H_V for our simulations is shown Figure 6. At the moment of the eruption's onset, no threshold is observed in the E_j/E_V ratio (Figure 6(a)); the different values have a dispersion of about 10% of the run with the highest value.

The situation is significantly different when the H_j/H_V ratio is considered. In fact, as shown in Figure 6(b), all the curves approach the same threshold value within a dispersion of about 3%. This dispersion range is between three and eight times smaller than the equivalent ranges in the different energies and helicities decompositions discussed in the previous Section, and about three times smaller than the E_j/E_V ratio. We note that this dispersion is (1) within the measurement precision of the helicity ratio, which is about 4% (see Section 3), hence basically the same value, and (2) it is about a factor two smaller than the dispersion of critical decay index values identified through the detailed analysis of the electric currents and magnetic field distribution in the different simulations (see Zuccarello et al. 2015).

7. Discussion and Conclusion

We have presented a series of eruptive and non-eruptive numerical MHD simulations of idealized solar active regions, which evolution is characterized by different boundary motions. With these series of simulations, we aimed at addressing (1) which of the different boundary motions are the most efficient to inject different decompositions of magnetic energy and helicity, and (2) whether any of the different energy and helicity decompositions are able to identify the moment of the onset of the eruptions.

The initial configuration consisted of an asymmetric, current-free, bipolar active region embedded in a constant Alfvèn speed atmosphere.

During the first phase of the simulation runs, called the shearing phase, shearing motions have been applied in the proximity of the active region's PIL. As a result, the coronal magnetic field evolves from a potential field into a current-carrying magnetic field characterized by a sheared arcade close to the PIL.

Starting from this configuration, four different classes of boundary motions, resembling motions often observed on the Sun, have been applied. This phase was called the flux rope formation phase. While the applied motions are relatively different among them, a characteristic that is common to all four motions is that they advect part of the photospheric

magnetic flux toward the PIL. During this flux rope formation phase, a change in the topology of the system is observed and a magnetic flux rope is formed, which eventually erupts (Zuccarello et al. 2015).

By analysing the time evolution of the different magnetic energy and helicity decompositions during the sharing and flux rope formation phases we have shown that:

1. Magnetic energy and total relative helicity are mostly injected during the shearing phase. The magnetic energy actually shows a significant decrease during the flux rope formation phase. This is due essentially to the decrease of the potential magnetic energy of the system, probably due the fact that magnetic flux is canceled at the PIL during the flux rope formation phase.

2. Shearing motions are the most efficient to inject E_j into the system. The injection rate of E_j during this phase is at least four times larger than during the flux rope formation phases.

3. The current-carrying component of the magnetic helicity, H_j, increases with a similar rate between the shearing and the flux rope formation phases.

In order to determine if any signature of the eruption's onset could be found in any of the magnetic energy or helicity decompositions, we analyzed the evolution of these quantities around the moment of the onset of the eruption, to investigate if a threshold in any of these quantities exists. Our analysis showed that:

1. No threshold is observed for any of the quantities entering in the decomposition of the magnetic energy (Equation (3)) and relative helicity (Equation (6)). In the different simulations, the eruption occurs for various values of energies and helicities. The dispersion of these values is between 9% and 25% depending on the particular decomposition (with helicities decomposition in the lower part of this range).

2. A threshold appears to exist in the ratio between the current-carrying component of the magnetic helicity and the total relative magnetic helicity. The onset of the eruptions indeed occurs when the different eruptive simulations reach the very same value of H_j/H_V, within measurement precision. This is not the case when a similar ratio in energies, i.e., E_j/E, is considered.

Pariat et al. (2017) have already discussed the promising properties of the ratio H_j/H_V, as possible eruptivity proxy. The numerical experiments set-up was however limited in the sense that it could not conclude on the existence of a threshold, as the magnetic systems were not driven to instability in a controlled way from a stable configuration. This caveat is lifted for the numerical experiments analyzed in the present study.

For the same simulations discussed in this paper, Zuccarello et al. (2015) performed a detailed analysis of the current distributions as well as several relaxation runs to determine the onset of the eruption. These authors have concluded that the driver of the eruption is indeed the torus instability; however, different simulations had a slightly different critical values of the decay index. They found that the critical value of the decay index at the onset of the eruptions is in the range $n_{critical} \in [1.4, 1.5]$.

The torus instability occurs when the magnetic pressure of the current-currying flux rope is not balanced by the magnetic tension of the magnetic field "external" to it. The condition for the instability has been first derived analytically using infinitesimal current rings. It has been shown that the instability occurs when the apex of the current ring is in a location where the decay index is $n \gtrsim n_{critical} = 1.5$ (Bateman 1978; Kliem & Török 2006; Démoulin & Aulanier 2010). There are several reasons why the critical decay index may differ among the different simulations: slightly different flux rope morphologies, limitations in determining the axis of nonanalytical flux ropes and slightly different line-tying effects being the most relevant. Nevertheless, the clear result of Zuccarello et al. (2015) was that when the flux rope's axis has reached an height where the decay index is $n \simeq 1.45 \pm 0.05$ a full eruption occurs. This value is remarkably close to the critical value for an idealized current ring.

The helicity of the current-carrying component of the magnetic field, H_j, is only related to the distribution of the electric currents. On the other hand, H_V also accounts for the contribution of the interaction between this magnetic field and the potential field. The ratio H_j/H_V estimates the importance of H_j over H_V, i.e., the importance of the field only associated with the currents over the total field. In our simulations, the torus instability occurs when the current-carrying flux rope has enough magnetic pressure that cannot be balanced by the tension of the potential field associated with the given boundary. For the present simulation set-up, when this occurs H_j is about one-third of H_V, i.e., enough currents, associated with twisted, pressure-carrying magnetic fields, have been accumulated and they cannot be balanced any more by the tension of the potential field associated with the given boundary.

In this paper, we have shown that at the moment of the onset of the torus instability, the ratio $H_j/H_V \simeq 0.29 \pm 0.01$ for four different simulations of torus unstable flux ropes. This suggests that the ratio H_j/H_V is a good proxy for the onset of the torus instability, at least for this set of simulations. Some caution should however be taken in interpreting the particular value of 0.29. Relative magnetic helicity, as defined in this study, is not a simply additive quantity. It implies that had the helicities been computed in a different volume, using different boundary locations, a different value of the helicity threshold may have been obtained. In the present study, the values obtained between the simulations are consistent with each other, because they are computed on the very same numerical domain, which robustly validates the core results of the existence of a threshold on H_j/H_V for these simulations. The specific value obtained is however likely not universal. This value should not be taken straightforwardly as an eruption trigger criteria in, for example, observational studies, before further studies have been carried out. Relative magnetic helicity remains a poorly understood physical quantity that may need to be theoretically partly redefined and whose properties need to be further understood (e.g., as in Demoulin et al. 2006; Yeates & Hornig 2013; Dalmasse et al. 2014; Russell et al. 2015; Aly 2018; Dalmasse et al. 2018; Oberti & Ricca 2018).

If the ratio H_j/H_V turns out to be either physically related to the torus instability or just a good proxy of it, this would constitute a significant step forward in forecasting solar eruptions. In fact, the determination of the eruptivity potential of an active region based on the evaluation of the decay index can be achieved through observations (Kliem et al. 2013; Zuccarello et al. 2014, 2016; James et al. 2018). However, its

routine application might not be straightforward: it requires one to address nontrivial problems such as defining and identifying the axis of nonanalytical flux ropes in strongly asymmetric configurations and inferring the three-dimensional nature of solar filaments from stereoscopic observations. On the other hand, evaluating the ratio H_j/H_V would only require the construction of a three-dimensional magnetic field model of the active region, the automation of which could be achieved more easily than the other approach. However, before considering all of the above, the robustness of this criterion, whether or not the threshold effectively exists, and if its value is magnetic-system independent, needs to be extensively tested, first using as many numerical experiments as possible, and then against observed data.

ORCID iDs

Francesco P. Zuccarello https://orcid.org/0000-0003-0320-7528
E. Pariat https://orcid.org/0000-0002-2900-0608
G. Valori https://orcid.org/0000-0001-7809-0067

References

Aly, J.-J. 2018, FlDyR, 50, 011408
Aulanier, G., Démoulin, P., & Grappin, R. 2005, A&A, 430, 1067
Aulanier, G., Török, T., Démoulin, P., & DeLuca, E. E. 2010, ApJ, 708, 314
Bateman, G. 1978, MHD Instabilities (Cambridge, MA: MIT Press)
Berger, M. A. 1984, GApFD, 30, 79
Berger, M. A. 2003, in Topological Quantities in Magnetohydrodynamics, ed. A. Ferriz-Mas & M. Núñez (London: Taylor & Francis), 345
Berger, M. A., & Field, G. B. 1984, JFM, 147, 133
Brandenburg, A., Petrie, G. J. D., & Singh, N. K. 2017, ApJ, 836, 21
Chae, J. 2001, ApJL, 560, L95
Dalmasse, K., Pariat, E., Démoulin, P., & Aulanier, G. 2014, SoPh, 289, 107
Dalmasse, K., Pariat, É., Valori, G., Jing, J., & Démoulin, P. 2018, ApJ, 852, 141
Démoulin, P., & Aulanier, G. 2010, ApJ, 718, 1388
Démoulin, P., & Pariat, E. 2009, AdSpR, 43, 1013
Demoulin, P., Pariat, E., & Berger, M. A. 2006, SoPh, 233, 3
Démoulin, P., Priest, E. R., & Lonie, D. P. 1996, JGR, 101, 7631
Finn, J. M., & Antonsen, T. M. 1985, CoPPC, 9, 111
Green, L. M., Démoulin, P., Mandrini, C. H., & van Driel-Gesztelyi, L. L. 2003, SoPh, 215, 307
Green, L. M., López Fuentes, M. C., Mandrini, C. H., Démoulin, P., & van Driel-Gesztelyi, L. L. 2002, SoPh, 208, 43
Guo, Y., Pariat, E., Valori, G., et al. 2017, ApJ, 840, 40
James, A. W., Valori, G., Green, L. M., et al. 2018, ApJL, 855, L16
Karpen, J. T., DeVore, C. R., Antiochos, S. K., & Pariat, E. 2017, ApJ, 834, 62
Kliem, B., Lin, J., Forbes, T. G., Priest, E. R., & Török, T. 2014, ApJ, 789, 46
Kliem, B., Su, Y. N., van Ballegooijen, A. A., & DeLuca, E. E. 2013, ApJ, 779, 129
Kliem, B., & Török, T. 2006, PhRvL, 96, 255002
Knizhnik, K. J., Antiochos, S. K., & DeVore, C. R. 2015, ApJ, 809, 137
Knizhnik, K. J., Antiochos, S. K., & DeVore, C. R. 2017, ApJ, 835, 85
LaBonte, B. J., Georgoulis, M. K., & Rust, D. M. 2007, ApJ, 671, 955
Leake, J. E., Linton, M. G., & Antiochos, S. K. 2014, ApJ, 787, 46
Leake, J. E., Linton, M. G., & Török, T. 2013, ApJ, 778, 99
Liu, Y., Hoeksema, J. T., Bobra, M., et al. 2014a, ApJ, 785, 13
Liu, Y., Hoeksema, J. T., & Sun, X. 2014b, ApJL, 783, L1
Liu, Y., & Schuck, P. W. 2012, ApJ, 761, 105
Low, B. C. 1996, SoPh, 167, 217
Mandrini, C. H., Pohjolainen, S., Dasso, S., et al. 2005, A&A, 434, 725
Miesch, M. S., Zhang, M., & Augustson, K. C. 2016, ApJL, 824, L15
Moraitis, K., Tziotziou, K., Georgoulis, M. K., & Archontis, V. 2014, SoPh, 289, 4453
Nindos, A., & Andrews, M. D. 2004, ApJL, 616, L175
Nindos, A., & Zhang, H. Q. 2002, ApJL, 573, L133
Oberti, C., & Ricca, R. L. 2018, FlDyR, 50, 011413
Olmedo, O., & Zhang, J. 2010, ApJ, 718, 433
Pariat, E., Leake, J. E., Valori, G., et al. 2017, arXiv:1703.10562
Pariat, E., Valori, G., Démoulin, P., & Dalmasse, K. 2015, A&A, 580, A128
Park, S.-H., Chae, J., & Wang, H. 2010, ApJ, 718, 43
Park, S.-H., Cho, K. S., Bong, S.-C., et al. 2012, ApJ, 750, 48
Park, S.-H., Lee, J., Choe, G. S., et al. 2008, ApJ, 686, 1397
Priest, E. R., Longcope, D. W., & Janvier, M. 2016, SoPh, 291, 2017
Prior, C., & Yeates, A. R. 2014, ApJ, 787, 100
Romano, P., Zuccarello, F. P., Guglielmino, S. L., & Zuccarello, F. 2014, ApJ, 794, 118
Rudenko, G. V., & Myshyakov, I. I. 2011, SoPh, 270, 165
Russell, A. J. B., Yeates, A. R., Hornig, G., & Wilmot-Smith, A. L. 2015, PhPl, 22, 032106
Rust, D. M., & Kumar, A. 1994, SoPh, 155, 69
Smyrli, A., Zuccarello, F., Romano, P., et al. 2010, A&A, 521, A56
Sturrock, Z., & Hood, A. W. 2016, A&A, 593, A63
Sturrock, Z., Hood, A. W., Archontis, V., & McNeill, C. M. 2015, A&A, 582, A76
Thalmann, J. K., Inhester, B., & Wiegelmann, T. 2011, SoPh, 272, 243
Török, T., & Kliem, B. 2007, AN, 328, 743
Tziotziou, K., Georgoulis, M. K., & Liu, Y. 2013, ApJ, 772, 115
Tziotziou, K., Georgoulis, M. K., & Raouafi, N.-E. 2012, ApJL, 759, L4
Tziotziou, K., Tsiropoula, G., Georgoulis, M. K., & Kontogiannis, I. 2014, A&A, 564, 86
Valori, G., Démoulin, P., & Pariat, E. 2012, SoPh, 278, 347
Valori, G., Démoulin, P., Pariat, E., & Masson, S. 2013, A&A, 553, 38
Valori, G., Pariat, E., Anfinogentov, S., et al. 2016, SSRv, 201, 147
van Driel-Gesztelyi, L. L., & Green, L. M. 2015, LRSP, 12, 1
Yang, S., Büchner, J., Santos, J. C., & Zhang, H. Q. 2013, SoPh, 283, 369
Yeates, A. R., & Hornig, G. 2013, PhPl, 20, 012102
Yeates, A. R., & Hornig, G. 2014, Journal of Physics: Conference Series, 544, 012002
Yeates, A. R., & Hornig, G. 2016, A&A, 594, A98
Zhao, L., DeVore, C. R., Antiochos, S. K., & Zurbuchen, T. H. 2015, ApJ, 805, 61
Zuccarello, F. P., Aulanier, G., & Gilchrist, S. A. 2015, ApJ, 814, 126
Zuccarello, F. P., Aulanier, G., & Gilchrist, S. A. 2016, ApJL, 821, L23
Zuccarello, F. P., Chandra, R., Schmieder, B., Aulanier, G., & Joshi, R. 2017, A&A, 601, A26
Zuccarello, F. P., Romano, P., Zuccarello, F., & Poedts, S. 2011, A&A, 530, A36
Zuccarello, F. P., Seaton, D. B., Mierla, M., et al. 2014, ApJ, 785, 88